# High-spin structure of the *sd* shell nuclei $^{25}$Na and $^{22}$Ne

J. Williams,[1,*] G. C. Ball,[1] A. Chester,[2,†] P. Choudhary,[3] T. Domingo,[2] A. B. Garnsworthy,[1] G. Hackman,[1] J. Henderson,[1,‡] R. Henderson,[1] R. Krücken,[1,4] R. S. Lubna,[1] J. Measures,[1,5] O. Paetkau,[1] J. Park,[1,4,§] J. Smallcombe,[1,¶] P. C. Srivastava,[3] K. Starosta,[2] C. E. Svensson,[6] K. Whitmore,[2] and M. Williams[1]

[1] *TRIUMF, 4004 Wesbrook Mall, Vancouver, British Columbia, Canada V6T 2A3*
[2] *Department of Chemistry, Simon Fraser University, 8888 University Drive, Burnaby, British Columbia, Canada V5A 1S6*
[3] *Department of Physics, Indian Institute of Technology Roorkee, Roorkee, Uttarakhand, India 247667*
[4] *Department of Physics & Astronomy, University of British Columbia, Vancouver, British Columbia, Canada V6T 1Z4*
[5] *Department of Physics, University of Surrey, Guildford, Surrey, United Kingdom GU2 7XH*
[6] *Department of Physics, University of Guelph, Guelph, Ontario, Canada N1G 2W1*

(Dated: November 17, 2020)

The level structure of $^{25}$Na and $^{22}$Ne in the high excitation energy/high spin regime was studied using gamma-ray spectroscopy and Doppler shift lifetime measurements following $^{12}$C($^{18}$O,$\alpha p$)$^{25}$Na and $^{12}$C($^{18}$O,2$\alpha$)$^{22}$Ne reactions. Multiple new levels and transitions were identified in both nuclides based on $\gamma-\gamma$ coincidence data. In $^{25}$Na, evidence was found for higher-spin negative-parity states up to $I^{\pi} = 13/2^{-}$ resulting from neutron excitation into the $pf$ shell, in good agreement with shell model calculations using the SDPF-MU and FSU interactions. Candidates for the yrast $7^{+}$ and $8^{+}$ levels in $^{22}$Ne, consistent with calculations using the USDB interaction, were also identified.

## I. INTRODUCTION

Nuclear structure studies at the limits of high spin and excitation energy provide a sensitive probe of shell evolution. Even in nuclei relatively close to stability, it is possible to study phenomena which manifest at low energy in more exotic nuclei, since states formed at high excitation energy will often involve couplings of the same single-particle orbitals which lie at the Fermi surface of nuclei further from stability. For instance, it is now well known that the $N = 20$ shell gap vanishes for neutron-rich Na and Mg isotopes due to the tensor force driving deformation and leading to an "island of inversion" defined by ground state population of neutron $pf$ intruder orbitals [1–3]. As a result, several recent studies in this region have investigated the potential for cross-shell excitations in nearby less neutron-rich species, typically using fusion-evaporation reactions to access the higher energy and spin regime where intruder states are expected to reside [4–7]. Similar investigations of lower and mid *sd* shell nuclei such as $^{25}$Na can provide access to negative parity intruder states from multiple cross-shell excitation modes - proton or neutron excitation out of the $p$ shell below or neutron excitation into the $pf$ shell above. Comparisons of observed intruder states to shell model predictions in the $psdpf$ valence space can be used to assist in determination of their cross-shell excitation modes and to assess the accuracy of those models for predicting cross-shell excitations in the high energy and spin regime.

This study investigates the structure of $^{25}$Na and $^{22}$Ne using a fusion-evaporation reaction to populate states at high spin and excitation energy. The higher-spin structure of $^{25}$Na has previously been studied using the $^{9}$Be($^{18}$O,$pn$) fusion-evaporation reaction at $E_{beam} =$ 35 MeV, revealing several previously unobserved levels and transitions [8]. In this work, a more symmetric $^{12}$C($^{18}$O,$\alpha p$) reaction is used at a higher beam energy to investigate yrast states closer to the neutron separation energy. A detailed study of the $2\alpha$ channel populating the stable nuclide $^{22}$Ne is also performed. Previous studies of high-spin levels in $^{22}$Ne have been limited to alpha capture on $^{18}$O [9, 10], and light ion transfer reactions [11–13]. The $^{12}$C($^{18}$O,2$\alpha$) reaction is used in this study to search for additional high-spin states and to better characterize the yrast structure at $I > 6$.

## II. EXPERIMENTAL DETAILS

Both $^{25}$Na and $^{22}$Ne were produced in the same experiment using the $^{12}$C($^{18}$O,$\alpha p$) and $^{12}$C($^{18}$O,2$\alpha$) reaction channels, with a beam energy of 48 MeV. Gamma rays were detected using the TRIUMF-ISAC gamma-ray escape suppressed spectrometer (TIGRESS) [14], which was populated with 13 Compton suppressed high purity germanium (HPGe) clovers: 4 at 45°, 5 at 90°, and 4 at 135°. Charged particle detection was performed using a 38-element array of CsI(Tl) scintillators positioned downstream from the target, which is a subset of the larger CsI ball array developed as part of the TIGRESS Integrated Plunger (TIP) infrastructure [15]. Pulse shape analysis of CsI(Tl) waveforms was used to classify hits by charged particle type using the method of Ref. [16]. Fusion-evaporation data of interest was separated from

* ewilliams@triumf.ca
† Present address: National Superconducting Cyclotron Laboratory, 640 South Shaw Lane, East Lansing, MI, USA 48824
‡ Present address: Lawrence Livermore National Laboratory, 7000 East Ave, Livermore, CA, USA 94550
§ Present address: Center for Exotic Nuclear Studies, Institute for Basic Science, 34126 Daejeon, Republic of Korea
¶ Present address: Department of Physics, University of Liverpool, Liverpool, UK L69 3BX

random background events using a series of timing gates requiring 2 CsI(Tl) hits and 2 TIGRESS hits in coincidence.

The beam time was split between two $^{nat.}$C reaction targets described in Ref. [7]: a thin target which was primarily used to collect data for $\gamma - \gamma$ coincidence spectroscopy, and a backed target which was primarily used to determine electromagnetic transition rates via the Doppler Shift Attenuation Method (DSAM) [17]. Lineshapes in the backed target data were compared to lineshapes generated from simulations based on the GEANT4 framework [18], and the best fit lifetimes were obtained using the likelihood-ratio $\chi^2$ analysis method described in Ref. [19]. For the lineshape comparison, experimental and simulated data were assigned into six groups based on the average simulated Doppler shift factor $D = E_{det}/E_0$ for each unique combination of TIGRESS cores and CsI(Tl) detectors, as in Refs. [7, 19]. In cases where a level was fed by an intense transition, a feeding correction was applied by gating on the feeding transition and comparing its coincidence projection to a simulation of the corresponding cascade, as described in Ref. [20].

The uncertainty in the DSAM measurements associated with the stopping process was derived from a comparison of simulations using electronic stopping powers from ICRU report 73 (the GEANT4 default stopping model) [21] and SRIM-2013 [22]. Many DSAM studies in this region predate the stopping models used in this work, and instead use scaled experimental measurements - for example the stopping measurements of Ref. [23] used in [24–26]. A direct comparison of measured stopping powers in gold from Ref. [23] to values obtained from the ICRU73 and SRIM-2013 models in the energy range of interest for this work (recoil $E/A < 1$ MeV) is shown in Figure 1. A significant disagreement between both models and the experimental values occurs around $E/A = 0.9$ MeV for both Ne and Na ions, and the predictions of the two models diverge at lower energies. It is evident that there is significant systematic uncertainty associated with the choice of a stopping model. For intense transitions not limited by statistics, lifetimes determined using the ICRU73 model were typically shorter than those determined using the SRIM-2013 model, with disagreement on the order of 5-20 %. For several transitions in the species of interest, it is expected that there will be a significant fraction of events where the excited recoil fully stops in the target backing prior to $\gamma$-decay. For these transitions, the extrapolation of the stopping powers to very low energies has a significant effect on the inferred lifetime values. In this low energy regime, the stopping measurements of Ref. [23] generally fall between the ICRU73 and SRIM-2013 models. For this reason, the mean lifetime values reported in this work were taken as the unweighted mean of lifetime values derived using the ICRU73 and SRIM-2013 stopping models.

The geometry of the TIGRESS array provides six axially-symmetric rings of HPGe cores, three upstream

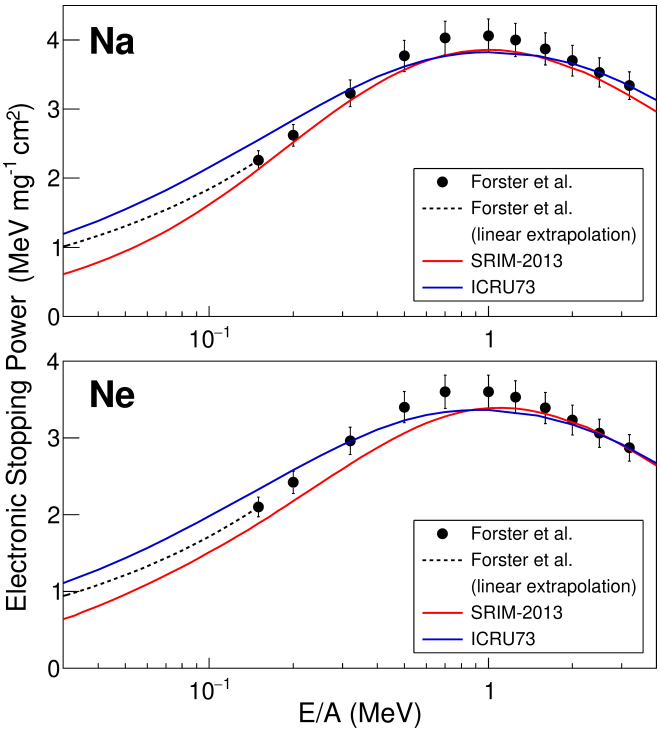


FIG. 1. (Color online) Comparison of electronic stopping powers in gold from the ICRU73 [21] and SRIM-2013 [22] models, and the scaled measurements of Forster *et al.* (Ref. [23], uncertainties of 6% are assumed). Linear extrapolations (in velocity) from the lowest Ref. [23] values to zero are shown as dashed lines.

of $\theta = 90°$ and three mirrored downstream, allowing the analysis of gamma ray angular distributions. Angular distribution data for intense transitions was fitted to a truncated series of Legendre polynomials under the assumption that all observed transitions were $E2$ or lower multipolarity:

$$W(\theta) = 1 + a_2 P_2(cos\ \theta) + a_4 P_4(cos\ \theta), \qquad (1)$$

where a negative $a_2$ value and $a_4 \approx 0$ is consistent with a stretched dipole ($M1$ or $E1$) transition, a positive $a_2$ value and a negative $a_4$ value is consistent with a stretched quadrupole ($E2$) transition or a mixed $M1/E2$ transition with $\Delta I = 0$, and a positive $a_4$ value is consistent with a mixed $M1/E2$ transition. For the low statistics data obtained for many of the high-lying transitions populated in this study, Equation 1 was truncated to the first two terms and only the $a_2$ term was determined.

## III. RESULTS

Observed levels in $^{25}$Na are reported in Table I along with a comparison to levels previously reported in Refs. [8, 27, 28]. The corresponding level scheme is shown in

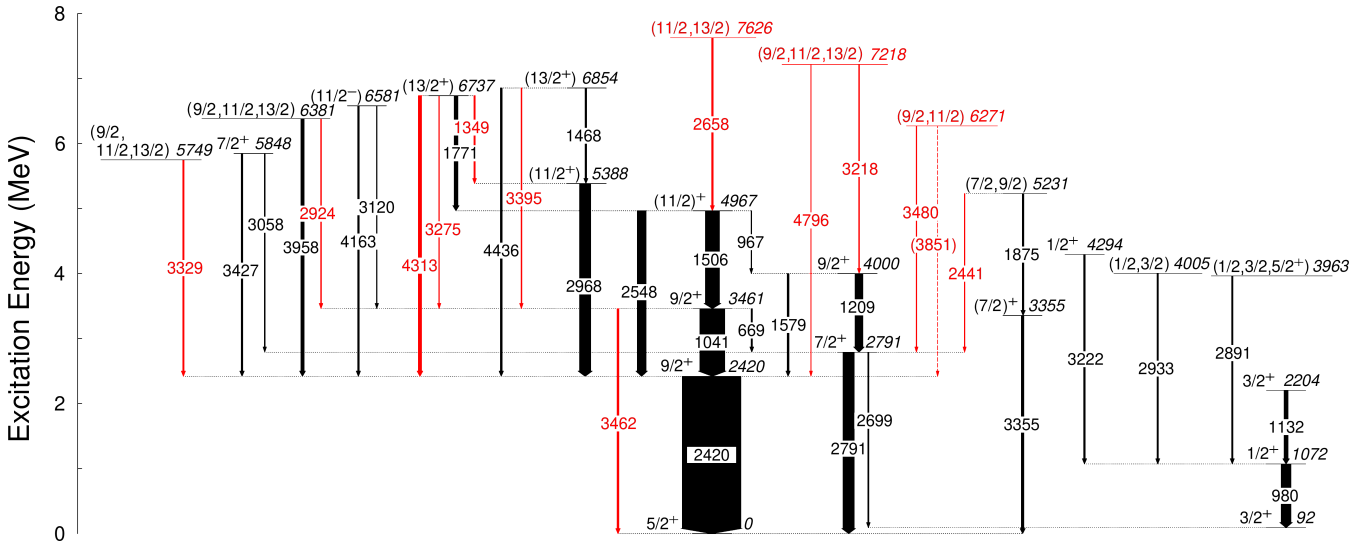


FIG. 2. (Color online) Scheme of observed levels and gamma rays in $^{25}$Na. Newly identified levels and gamma rays are highlighted in light red. Arrow widths specify relative intensities of gamma rays. Spin-parity values are taken from Table I and Refs. [8, 27, 28].

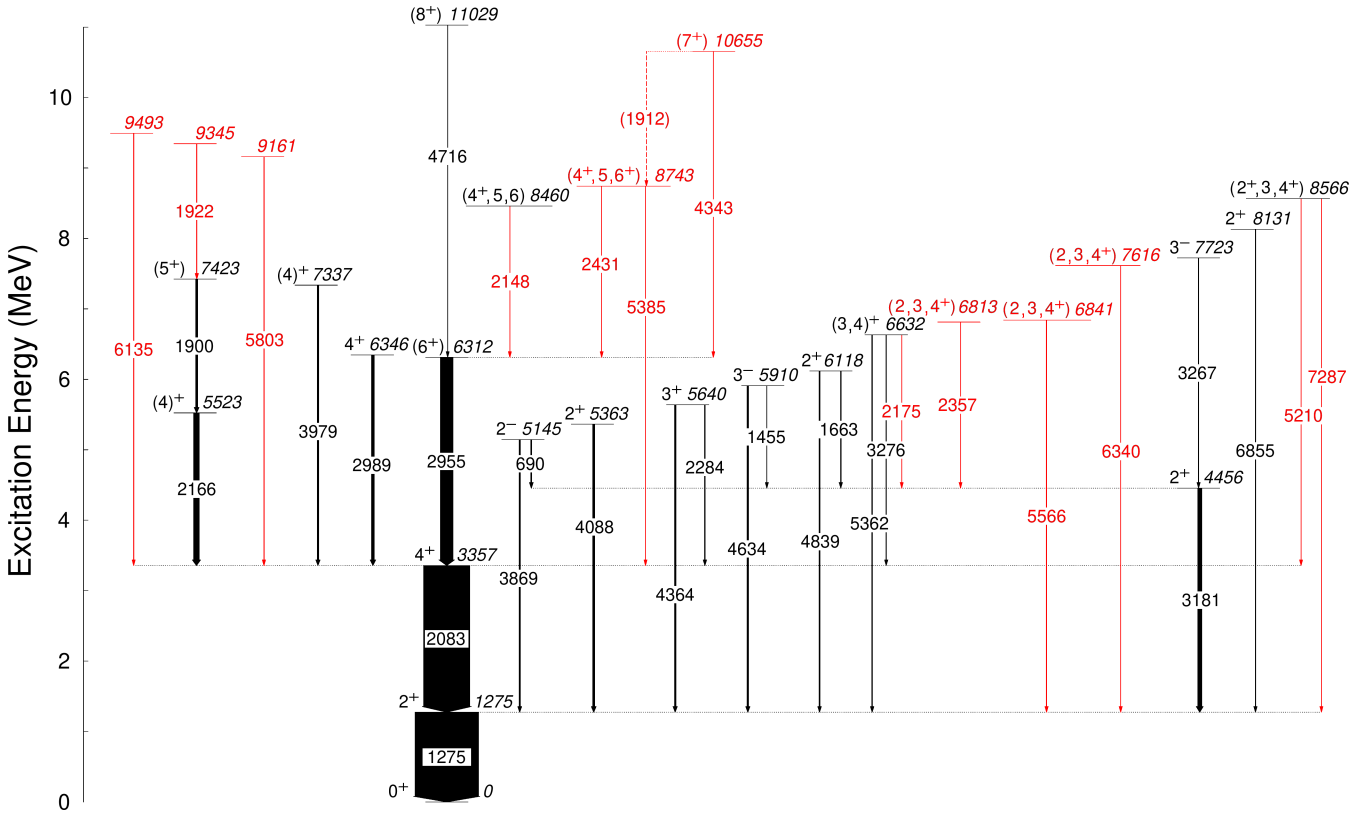


FIG. 3. (Color online) Scheme of observed levels and gamma rays in $^{22}$Ne. Newly identified levels and gamma rays are highlighted in light red. Arrow widths specify relative intensities of gamma rays. Spin-parity values are taken from Table II and Ref. [29].

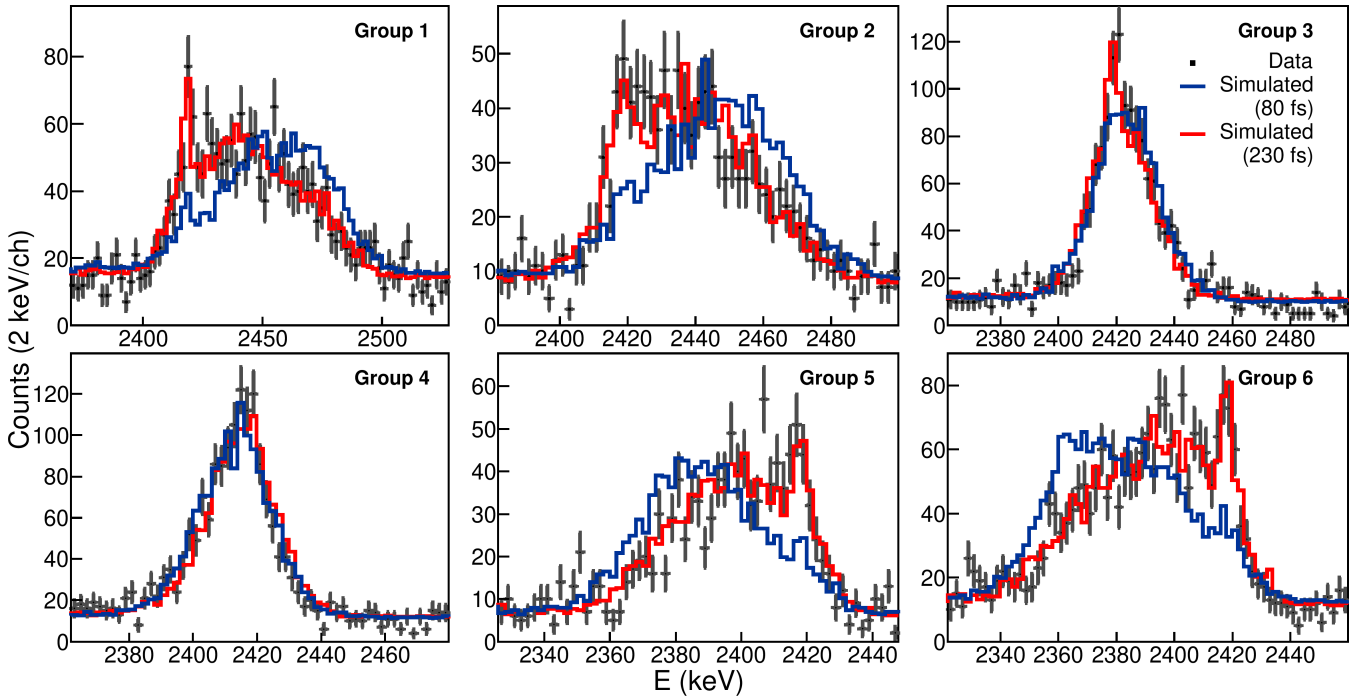


FIG. 4. (Color online) Comparison of backed target data for the 2419.6(11) keV transition in $^{25}$Na to GEANT4 simulated lineshapes for $\tau_{mean}$ = 80 and 230 fs using SRIM-2013 stopping powers. Group 1 contains detector combinations approximately corresponding to the most forward TIGRESS angles (highest $D$ values, see Section II). The simulated lineshapes for the two input lifetimes differ significantly in the intensity of the stopped component.

Figure 2. Observed levels in $^{22}$Ne are reported in Table II, and are compared to data previously reported in Ref. [29]. The $^{22}$Ne level scheme is shown in Figure 3. All reported level energies are based on observed transition energies corrected for gamma-ray recoil. For all transitions, $a_2$ coefficients (with $a_4$ fixed to zero) are reported in Tables I and II, while both $a_2$ and $a_4$ values are reported for select high-intensity transitions in Table III.

Many levels at high excitation energies in both $^{25}$Na and $^{22}$Ne were either too short-lived or not populated with sufficient statistics to constrain the lifetime from the DSAM lineshape analysis. In these cases, lifetime limits are reported using a 90% confidence interval. For higher intensity transitions, uncertainties in lifetime values were typically limited by the systematic uncertainty from the stopping process in the target. Figure 4 shows a comparison of the backed target data for the intense 2419.6(11) keV transition in $^{25}$Na to GEANT4 lineshapes simulated for $\tau_{mean}$ values of 80 and 230 fs using the ICRU73 model. For this transition, both stopped and shifted components of the lineshape are visible, with the relative intensities of these components depending on the transition rate.

### A. $^{25}$Na

The level scheme obtained for $^{25}$Na is largely consistent with the recent work of VonMoss *et al.* established from $^{9}$Be($^{18}$O,$np$)$^{25}$Na fusion-evaporation [8]. Most lifetimes determined from the DSAM lineshape analysis were slightly lower than those reported in Ref. [8], this is most likely a systematic effect resulting from the use of two stopping models in this work (as previously outlined in Section II), whereas Ref. [8] used the SRIM model exclusively. The present level scheme, shown in Figure 2, is slightly extended in excitation energy with 3 additional levels and 12 additional transitions identified. Angular distribution fits for selected transitions are shown in Figure 5. Additional details for individual states and transitions of interest are presented below.

There is a known $I^\pi = 3/2^+_1$ level in $^{25}$Na which is depopulated by a strong transition to the ground state and has been previously reported at 89.53(10) keV [28]. Although the transition to the ground state was not observed in this work, the presence of this level was inferred from transitions depopulating the observed levels at 1072(4) and 2791.0(12) keV. The level energy of 92(3) keV reported in this work is based on the energy difference of transitions depopulating the level at 2791.0(12) keV.

Consistent with Ref. [8], the strongest observed transitions belong to a band of high-spin states at 2419.8(11), 3460.9(9), and 4967.3(8) keV. Gamma-ray coincidence spectra for the transitions in this band are shown in Figures 6 and 7. Recent work by Knapton *et al.* using a $d$($^{24}$Na,$p$)$^{25}$Na reaction [27] has assigned $I^\pi = 9/2^+$ for

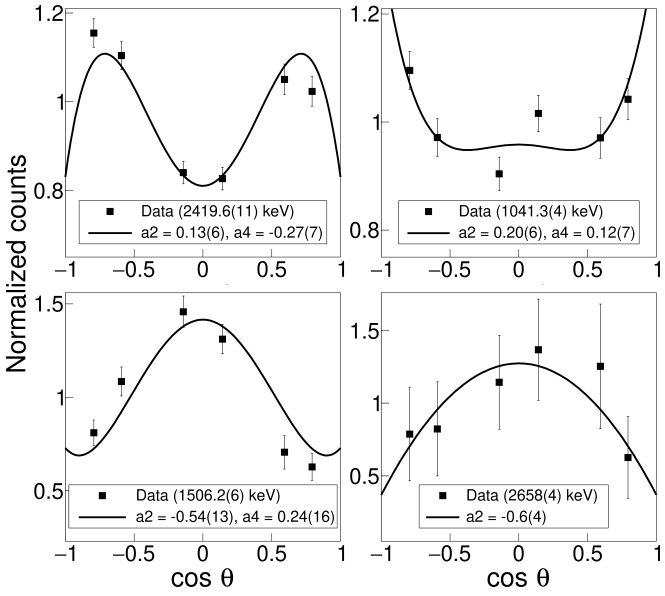


FIG. 5. Angular distribution fits for selected transitions in $^{25}$Na. For the low-intensity 2658(4) keV transition, the $a_4$ coefficient was fixed to zero.

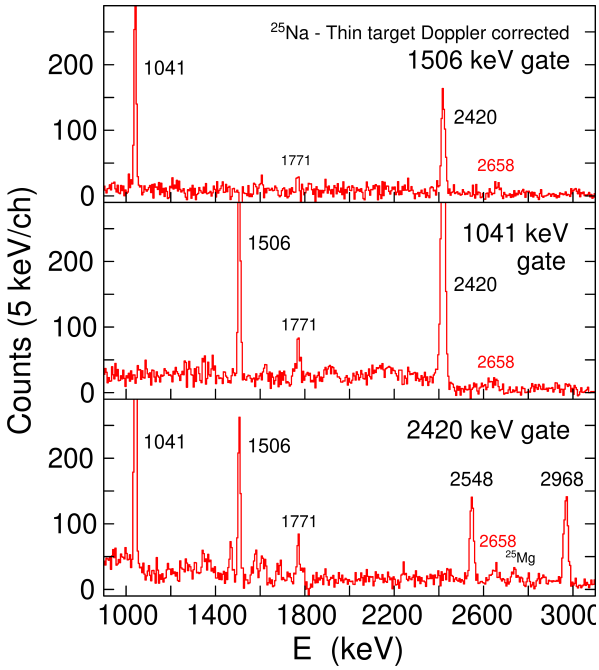


FIG. 6. (Color online) Background subtracted gamma-ray coincidence spectra from Doppler corrected thin target data, showing strong transitions in $^{25}$Na after gating on transitions in the main band. A newly identified transition at 2658(4) keV is highlighted in red.

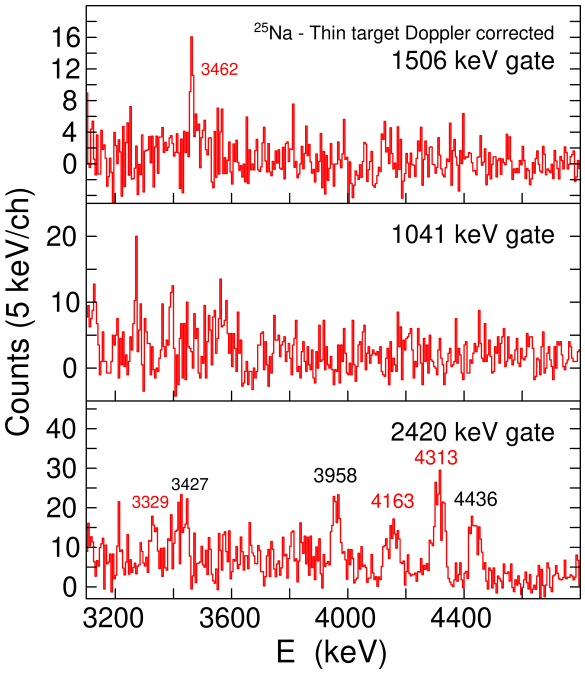


FIG. 7. (Color online) Background subtracted gamma-ray coincidence spectra from Doppler corrected thin target data, showing high energy transitions in $^{25}$Na after gating on transitions in the main band. Newly identified transitions are highlighted in red.

the lower two members of this band. The $9/2^+$ assignment for the 3460.9(9) keV level is further supported by observation of a weak transition from this level to the ground state, seen in Figure 7 at 3462(3) keV. Based on the low branching of the 3462(3) keV transition compared to the intense 1041.3(4) keV transition, it is likely that the transition to the ground state is pure E2 with the low energy transition being of mixed M1+E2 character. The intensity of the 3462(3) keV transition reported in Table I was corrected for summing effects using the method of Ref. [30]. Based on this analysis, it was determined that 10(2)% of the observed intensity of the 3462(3) keV transition originates from summing. Using the same method, the summing contributions to the 2548.0(12) and 4436(3) keV transitions were determined to be negligible ($< 1$ % of the observed intensity).

A secondary band containing low-spin states is populated, as evidenced by the strong 980.4(5) keV line which has previously been assigned as the $1/2^+_1 \rightarrow 3/2^+_1$ transition in $^{25}$Na. The $1/2^+_1$ level at 1072(4) keV is fed by several observed transitions, and it is likely the low-spin states here are fed from unobserved higher-lying, high-spin states.

For the side band containing levels at 2791.0(12) and 3999.6(11) keV, there is some disagreement in the literature regarding spin assignments and lifetimes. The present data suggests a shorter mean lifetime of 150(20) fs for the 2791.0(12) keV level, in disagreement with the value of 250(50) fs reported in the $^3$He($^{26}$Mg,$\alpha$) data of Ref. [26] but in reasonable agreement with the 190(35) fs value reported in the fusion-evaporation data of Ref. [8]. Feeding corrections were present in all measurements - the lifetime of the 2791.0(12) level reported in this work

is corrected for the observed feeding from the 3999.6(11) keV level. Additionally, the evaluated data of Ref. [28] suggests low spin parity values for the members of this band, in particular $I^\pi = 1/2^-$ for the 3999.6(11) keV level, which was derived from the $^{26}$Mg(d,t) data of Refs. [31, 32] (and which would also restrict the spin of the 2791.0(12) keV level to 5/2 or lower). These assignments disagree with the results from the present work and Ref. [8], since transitions from higher spin states to the 3999.6(11) keV level are observed. Since gamma-ray spectroscopy was not performed in Refs. [31, 32], it is possible that the $I^\pi = 1/2^-$ assignment instead belongs to another level with similar excitation energy, for instance the 4005(5) keV level in the lower-spin band.

Transitions belonging to a band with levels at 3355(3) and 5231(2) keV previously reported in Ref. [8] are also observed in this work. The relative intensities of these transitions are poorly constrained due to the presence of strong background lines near the 1875.0(12) and 3355(3) keV transitions in the ungated gamma ray spectra. The presence of both transitions was verified through $\gamma - \gamma$ gating. An additional weak transition connecting the 5231(2) keV level to the strongly populated 2791.0(12) keV level was also observed. Both transitions from the 5231(2) keV level populate levels with $I^\pi = (7/2^+)$, and it is unlikely that both transitions are pure E2 since the higher energy of the two transitions is significantly lower in intensity. This suggests that the 5231(2) keV level has $I = (7/2, 9/2)$, with the $I = 5/2$ case being much less likely due to preferential population of states near the yrast line from fusion-evaporation.

A new level at 6271(5) keV is inferred from a 3480(4) keV transition in coincidence with the strong 2790.8(13) keV transition in $^{25}$Na. There is likely a second transition from this level to the 2419.8(11) keV level, with a branching ratio $< 33$ %. The existence of this transition is inferred based on the presence of the 2419.6(11) transition in coincidence with a background-subtracted gate on the expected transition energy of 3851 keV, while it is absent when taking a gate 100 keV lower in energy. This evidence suggests that the 6271(5) keV level has $I = (9/2, 11/2)$, with the same reasoning as for the 5231(2) keV level.

A level is observed at 6581(2) keV which may correspond to a $I^\pi = (11/2^-)$ level identified by Knapton *et al.* using a $d(^{24}\text{Na},p)^{25}\text{Na}$ reaction, with excitation energy of 6.55(2) MeV determined using the SHARC silicon array [27]. Population of levels with this spin would be expected following fusion-evaporation, and the decay scheme observed for the $I^\pi = (11/2^-)$ level in Ref. [27] is consistent with the 6581(2) keV level from this work.

The level observed at 6854(2) keV is assigned $I^\pi = (13/2^+)$ based on the similar relative intensities of two transitions depopulating this level with significantly different transition energies (1467.9(10) and 4436(3) keV), assuming that the lower energy transition is primarily M1, while the higher energy transition is pure E2. Both assumptions are supported by the derived $a_2$ coefficients.

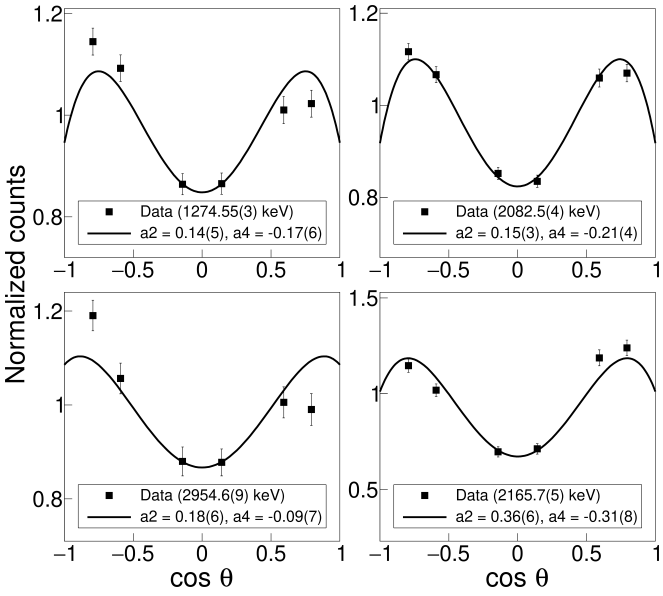


FIG. 8. Angular distribution fits for strongly populated transitions in $^{22}$Ne.

This assignment also implies that the level at 5388.4(18) keV should be assigned $I^\pi = (11/2^+)$.

A newly observed level at 7626(4) keV is inferred from a 2658(4) keV transition in coincidence with the 2419.6(11), 1041.3(4), 1506.2(6), and 2548.0(12) keV transitions (shown in Figure 6). The corresponding angular distribution (shown in Figure 5) is consistent with a M1 or mixed M1/E2 transition. The 7626(4) keV level is assigned $I = (11/2, 13/2)$ based on the $a_2$ coefficient, the assumption that the level is near-yrast, and non-observation of any direct transitions to the strongly populated $9/2^+_1$ and $9/2^+_2$ levels.

### B. $^{22}$Ne

The level scheme obtained for $^{22}$Ne contains a number of previously unobserved transitions. Many of the higher-lying levels were tentatively assigned spin and parity values based on the observed decay scheme and angular distribution coefficients. Angular distribution fits for intense transitions along the yrast band are shown in Figure 8. Gamma-ray spectra gated on the strong $4^+_1 \rightarrow 2^+_1$ and $2^+_1 \rightarrow 0^+_1$ transitions are shown in Figures 9 and 10. Additional details for states and transitions of interest are discussed below.

The DSAM lineshape analysis for the 4088.4(18) keV transition depopulating the 5363.4(18) keV level indicates that this level is short-lived with $\tau_{mean} < 4$ fs, in disagreement with Ref. [33] but in agreement with Ref. [34]. Additionally, the 5639.9(13) keV level lifetime of 20(8) fs derived from the DSAM lineshape analysis of the 4364(2) keV transition is in disagreement with the value $\tau_{mean} < 4$ fs reported in Ref. [33]. For both levels,

TABLE I. List of $^{25}$Na levels and gamma rays observed in this work, and measured $a_2$ angular distribution coefficients, mean lifetimes, and inferred spin-parities compared against recent values reported by Refs. [8, 26–28] where available.

| This work | | | | | | Previous results (see footnote) | |
|---|---|---|---|---|---|---|---|
| $E_{level}$ (keV) | $E_\gamma$ (keV) | $I_{\gamma,rel}$ | $a_2$ | $I^\pi$ | $\tau_{\rm mean}$ (fs) | $I^\pi$ | $\tau_{\rm mean}$ (fs) |
| 92(3) | - | - | - | - | - | $3/2^+$ [d] | $7.4(4)\times10^6$ [d] |
| 1072(4) | 980.4(5) | 0.170(14) | -0.7(3) | - | $>800$ † | $1/2^+$ [d] | 1900(200) [d] |
| 2204(4) | 1131.8(4) | 0.069(12) | -0.1(3) | - | 26(11) | $3/2^+$ [d] | 36(6) [d] |
| 2419.8(11) | 2419.6(11) | 1.00(3) | 0.30(3) | $(9/2^+)$ | 230(40) * | $9/2^+$ [c] | 240(40) [a] |
| 2791.0(12) | 2699(3) | 0.018(4) | 0.9(3) | - | 150(20) * | $7/2^+$ [c] | 190(35) [a] / 250(50) [b] |
| | 2790.8(13) | 0.192(15) | 0.39(14) | - | | | |
| 3355(3) | 3355(3) | 0.045(16) | -0.2(3) | - | $<49$ † | $(7/2)^+$ [a] | 23(7) [d] |
| 3460.9(9) | 669.1(7) | 0.022(3) | -0.4(2) | $(9/2^+)$ | 190(30) * | $9/2^+$ [c] | 210(25) [d] / 130(40) [a] |
| | 1041.3(4) | 0.427(11) | 0.12(3) | | | | |
| | 3462(3) | 0.032(11) | -0.1(7) | | | | |
| 3963(4) | 2891(3) | 0.026(9) | 0.0(5) | $(1/2,3/2,5/2^+)$ | $<250$ † | $(1/2^+,3/2,5/2^+)$ [d] | $<140$ [d] |
| 3999.6(11) | 1209.0(4) | 0.135(10) | -0.31(9) | - | 90(7) | $9/2^+$ [c] | 100(20) [a] |
| | 1579.1(13) | 0.028(4) | 0.0(3) | | | | |
| 4005(5) | 2933(3) | 0.026(9) | -0.8(6) | $(1/2,3/2)$ | 90(50) | - | 45(10) [d] |
| 4294(5) | 3222(3) | 0.030(10) | -0.4(7) | - | $<29$ † | $1/2^+$ [d] | - |
| 4967.3(8) | 967.3(9) | 0.011(3) | -0.2(5) | - | 72(6) * | $(11/2)^+$ [a] | |
| | 1506.2(6) | 0.244(10) | -0.70(8) | | | | 80(20) [a] |
| | 2548.0(12) | 0.140(9) | -0.03(13) | | | | 120(30) [a] |
| 5231(2) | 1875.0(12) | 0.04(2) | 0.3(2) | $(7/2,9/2)$ | $<15$ † | - | - |
| | 2441(3) | 0.009(3) | -0.9(9) | | | | |
| 5388.4(18) | 2968.4(15) | 0.170(10) | -0.15(13) | $(11/2^+)$ | $<4$ † | $(9/2,11/2)^+$ [a] | - |
| 5749(4) | 3329(4) | 0.016(3) | 0.1(4) | $(9/2,11/2,13/2)$ | $<280$ † | - | - |
| 5848(3) | 3058(3) | 0.014(3) | 0.9(5) | - | $<75$ † | $7/2^+$ [c] | - |
| | 3427(4) | 0.017(3) | 0.1(4) | | | | |
| 6271(5) | 3480(4) | 0.010(2) | -0.3(7) | $(9/2,11/2)$ | $<37$ † | - | - |
| | *3851(5)* | $<0.004$ | - | | | | |
| 6381(3) | 2924(5) | 0.018(5) | -0.6(8) | $(9/2,11/2,13/2)$ | $<9$ † | - | - |
| | 3958(4) | 0.037(4) | -0.1(2) | | | | |
| 6581(2) | 3120(4) | 0.020(4) | -0.2(7) | - | $<40$ † | $(11/2^-)$ [c] | - |
| | 4163(4) | 0.027(3) | -0.1(3) | | | | |
| 6736.6(19) | 1348.9(13) | 0.021(5) | 0.3(3) | $(13/2^+)$ | $<4$ † | - | - |
| | 1770.7(16) | 0.064(8) | -0.3(2) | | | | |
| | 3275(6) | 0.012(4) | -0.1(10) | | | | |
| | 4313(3) | 0.053(4) | 0.3(2) | | | | |
| 6854(2) | 1467.9(10) | 0.026(4) | -0.6(3) | $(13/2^+)$ | 60(40) | $(11/2,13/2)^+$ [a] | - |
| | 3395(5) | 0.015(4) | -0.7(7) | | | | |
| | 4436(3) | 0.031(3) | 0.5(4) | | | | |
| 7218(4) | 3218(4) | 0.012(3) | 0.6(4) | $(9/2,11/2,13/2)$ | $<140$ † | - | - |
| | 4796(9) | 0.006(2) | -1.4(13) | | | | |
| 7626(4) | 2658(4) | 0.027(5) | -0.6(4) | $(11/2,13/2)$ | $<75$ † | - | - |

* Corrected for feeding from an observed transition. † Limit reported to a 90% confidence level.
Previous results from Refs. [8] [a], [26] [b], [27] [c], [28] [d].

no feeding transitions were observed in this work and as such no feeding corrections were applied in the DSAM analysis.

Lifetimes of the 6312.0(10) and 6345.9(13) keV levels were determined simultaneously, since the transitions depopulating these levels overlapped in the DSAM target data, and no intense feeding transitions were observed for either level which precluded a gate from above. The sum of simulated lineshapes for both transitions (scaled by relative intensity) was compared to the observed lineshape, and the best fit lifetimes determined simultaneously using a 2-dimensional grid of $\chi^2$ values (see Appendix A of Ref. [20]).

Ref. [33] assigned a 1430.9 keV gamma ray depopulating the 7337(3) keV level, which was not observed in this work. This 1430.9 keV gamma ray was also not observed in $^{22}$F beta-decay [35], so it is possible that this transition may have been assigned incorrectly.

A new level at 6841(7) keV was inferred from observation of a low-intensity gamma-ray at 5566(7) keV (shown in Figure 10). There is a known $I^\pi = (1^+)$ level at 6853.5(16) keV [29] with a similar decay scheme.

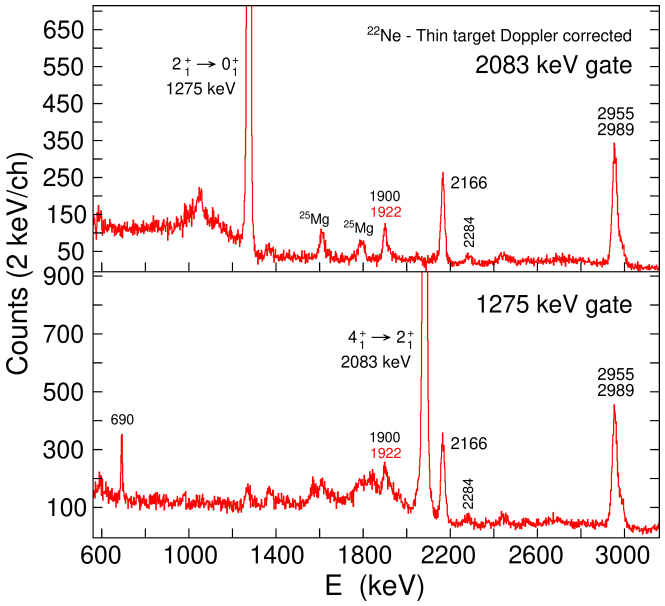


FIG. 9. (Color online) Background subtracted gamma-ray coincidence spectra from Doppler corrected thin target data, showing strong transitions in $^{22}$Ne. Newly identified transitions are highlighted in red.

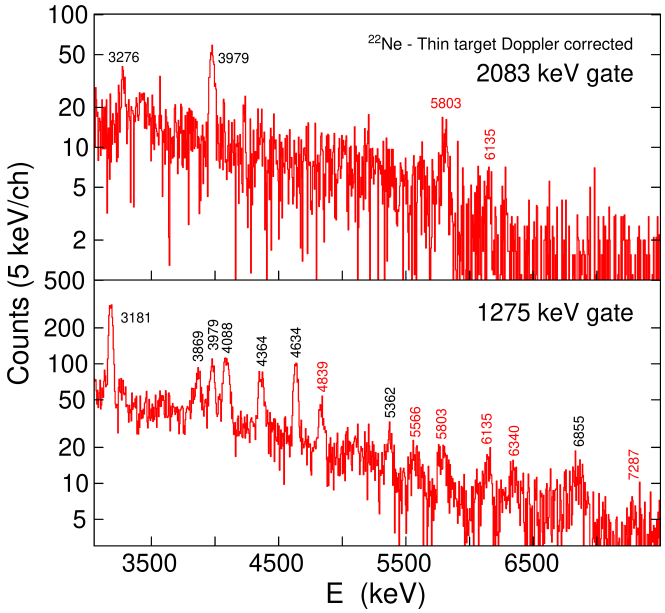


FIG. 10. (Color online) Background subtracted gamma-ray coincidence spectra from Doppler corrected thin target data, showing observed gamma rays in $^{22}$Ne at high energies. Newly identified transitions are highlighted in red.

However based on the level energy discrepancy and the tendency to populate higher-spin levels with fusion-evaporation, these are likely two separate levels.

A transition was observed at 6340(7) keV, which is at the approximate energy expected for a single escape peak of the 6855(7) keV transition depopulating the 8131(7) keV level. However these lines (both shown in Figure 10) are most likely two separate transitions, based on the similar intensities of the lines and the non-observation of escape peaks for any other transitions of similar energy. Based on this, a new level has been placed at 7616(7) keV in the level scheme.

A new level at 9344.6(18) keV is inferred from a 1921.5(15) keV transition to the 7423.0(9) keV level. When Doppler corrected, the 1921.5(15) and 1899.9(6) keV lines in this band partially overlap in energy. When gating in the region of this feature, the 2954.6(9) keV $6_1^+ \rightarrow 4_1^+$ transition and the 2431(4) keV transition to the $6_1^+$ level are observed. Since no transitions are observed linking the 5523-7423-9345 keV band to the $6_1^+$ level, this coincidence relationship is best satisfied by the presence of an additional low-intensity 1912 keV transition above the $6_1^+$ level, shown as a dashed line in Figure 3.

Two candidates for the yrast $8^+$ level were identified from high energy transitions in coincidence with the 2954.6(9) keV transition depopulating the $I^\pi = (6^+)$ level at 6312.0(10) keV, shown in Figure 11. A previously unobserved level at 10655(5) keV is inferred from a 4343(5) keV transition, and another level at 11029(4) keV was similarly inferred, consistent with the 11033 keV

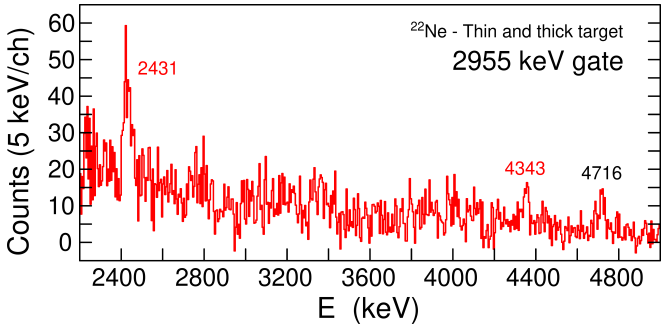


FIG. 11. (Color online) Background subtracted gamma-ray spectrum gated on the $6_1^+ \rightarrow 4_1^+$ transition in $^{22}$Ne, showing transitions depopulating levels at high excitation energy. Newly identified transitions are highlighted in red.

level reported in Ref. [36]. Both levels are slightly above the neutron separation energy $S_n = 10364.26(4)$ keV. The $a_2$ angular distribution coefficient for the 4343(5) keV transition is consistent with an E2 or mixed M1/E2 transition, whereas the angular distribution information for the 11029(4) keV level is inconclusive. These levels are assigned $I^\pi = (7^+)$ and $(8^+)$ based on the expected energy of the $8_1^+$ level based on $I(I+1)$ spacing for the yrast rotational band, the observed decay scheme, and the general expectation of increasing spin with excitation energy for states populated via fusion-evaporation.

TABLE II. List of $^{22}$Ne levels and gamma rays observed in this work, and measured $a_2$ angular distribution coefficients, mean lifetimes, and inferred spin-parities compared against evaluated data from Ref. [29].

| This work | | | | | | Ref. [29] | |
|---|---|---|---|---|---|---|---|
| $E_{level}$ (keV) | $E_\gamma$ (keV) | $I_{\gamma,rel}$ | $a_2$ | $I^\pi$ | $\tau_{\rm mean}$ (fs) | $I^\pi$ | $\tau_{\rm mean}$ (fs) |
| 1274.59(3) | 1274.55(3) | 1.000(15) | 0.25(3) | $(2^+)$ | $> 3500$ † | $2^+$ | 5190(70) |
| 3357.2(4) | 2082.5(4) | 0.747(13) | 0.30(2) | $(4^+)$ | 290(50) * | $4^+$ | 325(6) |
| 4455.7(10) | 3180.9(10) | 0.066(3) | 0.16(8) | - | $< 14$ † | $2^+$ | 5(4) |
| 5145.3(10) | 690.4(3) | 0.0161(15) | -0.31(17) | - | 1170(140) | $2^-$ | 1200(300) |
| | 3869.1(14) | 0.0162(16) | -0.78(16) | | | | |
| 5363.4(18) | 4088.4(18) | 0.032(2) | 0.02(9) | - | $< 4$ † | $2^+$ | 100(17) |
| 5523.0(6) | 2165.7(5) | 0.084(2) | 0.56(3) | - | 20(5) * | $(4)^+$ | 30(4) |
| 5639.9(13) | 2283.5(16) | 0.013(2) | -0.1(4) | - | 20(8) | $3^+$ | $< 4$ |
| | 4364(2) | 0.023(2) | -0.09(10) | | | | |
| 5910.3(10) | 1454.9(7) | 0.0040(8) | -0.1(3) | - | 71(16) | $3^-$ | 46(16) |
| | 4634.4(19) | 0.024(2) | -0.50(9) | | | | |
| 6117.8(15) | 1662.6(9) | 0.0091(19) | -0.7(4) | - | 24(16) | $2^+$ | 20(10) |
| | 4839(3) | 0.0111(13) | -0.09(15) | | | | |
| 6312.0(10) | 2954.6(9) | 0.206(5) | 0.24(3) | $(6^+)$ | 57(6) | $(6^+)$ | 71(6) |
| 6345.9(13) | 2988.5(12) | 0.044(2) | 0.21(13) | - | 16(5) | $4^+$ | 19(4) |
| 6632.4(19) | 2175(2) | 0.0028(7) | -0.3(7) | - | $< 240$ † | $(3,4)^+$ | 70(30) |
| | 3276(3) | 0.0055(10) | -0.3(4) | | | | |
| | 5362(5) | 0.0083(14) | -0.31(17) | | | | |
| 6812.8(17) | 2356.9(13) | 0.0019(6) | -0.3(6) | $(2,3,4^+)$ | $160^{+130}_{-90}$ | | |
| 6841(7) | 5566(7) | 0.0050(12) | -0.2(2) | $(2,3,4^+)$ | $< 380$ † | - | - |
| 7337(2) | 3979(2) | 0.025(2) | 0.17(10) | - | $< 26$ † | $(4)^+$ | 50(30) |
| 7423.0(9) | 1899.9(6) | 0.033(2) | -0.47(19) | - | $< 40$ † | $(5^+)$ | $< 4$ |
| 7616(7) | 6340(7) | 0.0052(10) | -0.4(2) | $(2,3,4^+)$ | $< 32$ † | - | - |
| 7723(2) | 3266.9(18) | 0.0056(11) | -0.5(6) | | $< 22$ † | $3^-$ | |
| 8131(7) | 6855(7) | 0.0071(11) | -0.6(2) | - | $< 31$ † | $2^+$ | - |
| 8460(3) | 2148(3) | 0.0056(12) | -0.7(16) | $(4^+,5,6)$ | $< 110$ † | - | - |
| 8566(5) | 5210(6) | 0.0038(8) | 0.0(4) | $(2^+,3,4^+)$ | $< 360$ † | - | - |
| | 7287(9) | 0.0020(7) | 0.7(5) | | | | |
| 8743(4) | 2431(4) | 0.0040(10) | -0.1(3) | $(4^+,5,6^+)$ | $< 40$ † | - | - |
| | 5385(7) | 0.0030(7) | -0.5(5) | | | | |
| 9161(5) | 5803(4) | 0.0069(12) | -0.02(18) | - | 70(30) | - | - |
| 9344.6(18) | 1921.5(15) | 0.0084(17) | 0.0(4) | - | $< 90$ † | - | - |
| 9493(7) | 6135(7) | 0.0050(10) | 0.0(3) | - | $< 270$ † | - | - |
| 10655(5) | *1912(7)* | $< 0.0037$ | - | $(7^+)$ | $< 120$ † | - | - |
| | 4343(5) | 0.0022(7) | 0.9(5) | | | | |
| 11029(4) | 4716(3) | 0.0017(9) | 0.5(6) | $(8^+)$ | $< 64$ † | $(6^+,8^+)$ | - |

* Corrected for feeding from an observed transition. † Limit reported to a 90% confidence level.

## IV. DISCUSSION

To further investigate the properties of observed levels, the experimental data was compared to predictions from various shell models including the phenomenological USDB interaction in the *sd* shell valence space [37], the YSOX interaction in the *psd* space [38], and the SDPF-MU interaction in the *sdpf* space [39]. In both the USDB and YSOX calculations, protons and neutrons were allowed to occupy all orbitals in the corresponding model space. The calculations using the SDPF-MU interaction were truncated to allow only single neutron excitation into the *pf* shell. Similar to the calculations in Ref. [7], effective charges $e_p = 1.5e$ and $e_n = 0.5e$ were used for the USDB and YSOX interactions. For the SDPF-MU interaction, the effective charge values $e_p = 1.35e$ and $e_n = 0.35e$ used in Ref. [39] were taken.

The aforementioned shell models were chosen to allow for investigation into cross-shell excitations, based on the results obtained when applying different restrictions to the model space. For the specific case of 1-particle 1-hole negative-parity states, further calculations were performed using the recent FSU interaction developed for the broader *spsdpf* space [40, 41]. In this study, the FSU calculations were truncated to the *psdpf* space, with the $^4$He core left intact.

TABLE III. Detailed angular distribution coefficient data for select transitions in $^{25}$Na and $^{22}$Ne. Transitions are classified as dipole (D) and/or quadrupole (Q).

| Nuclide | $E_\gamma$ (keV) | $a_2$ | $a_4$ | D/Q |
|---|---|---|---|---|
| $^{25}$Na | 2419.6(11) | 0.13(6) | -0.27(7) | Q |
| | 1041.3(4) | 0.20(6) | 0.12(7) | D+Q |
| | 1506.2(6) | -0.54(13) | 0.24(16) | D+Q |
| $^{22}$Ne | 1274.55(3) | 0.14(5) | -0.17(6) | Q |
| | 2082.5(4) | 0.15(3) | -0.21(4) | Q |
| | 2165.7(5) | 0.36(6) | -0.31(8) | D+Q, $\Delta I = 0$ |
| | 2954.6(9) | 0.18(6) | -0.09(7) | Q |

### A. $^{25}$Na

Low-lying positive-parity levels of $^{25}$Na were reproduced very well by each model tested (USDB, YSOX, and SDPF-MU - the FSU model is designed to give equivalent results to USDB for *sd* shell states). A comparison of the experimental data to the USDB calculations is shown in Figure 12. Observed levels which were not assigned to states predicted by USDB were compared to negative-parity states predicted using the YSOX, SDPF-MU, and FSU interactions in Figure 13. Each model predicts several negative-parity states above 5 MeV, indicating that both excitation out of the lower $p$ shell or into the upper $pf$ shell are possible. However, the former case is less likely to be populated in this study, since higher-spin states ($I > 9/2$) are not predicted from the YSOX calculations in the experimentally populated region.

The level observed at 7626(4) keV does not correspond well in energy to any of the levels predicted in the USDB calculations, and is therefore likely to be a negative-parity level. The YSOX calculations in the *psd* space predict some $I^\pi = 7/2^-, 9/2^-$ levels at similar energies, however the spin of the 7626(4) keV level is most likely 11/2 or higher, as discussed in Section III A. Higher-spin negative-parity states are predicted in the SDPF-MU and FSU calculations, where the 7626(4) keV level may correspond to either of the predicted $13/2^-_1$ or $11/2^-_2$ levels. A comparison of measured and predicted B(E1) values was carried out for the SDPF-MU calculations, under the assumption that the 7626(4) keV level is negative parity. As shown in Table IV, the calculations consistently under-predict B(E1) values (including known $(11/2^-) \rightarrow 9/2^+_2$ and $(11/2^-) \rightarrow 9/2^+_1$ transitions), however it is evident that the $13/2^-_1$ case best agrees with the observed transition depopulating the 7626(4) keV level. The $13/2^-_1$ case also agrees best with the energy systematics between observed levels and those predicted by the SDPF-MU and FSU interactions, as shown in Figure 13.

Since $^{25}$Na is positioned in the mid-*sd* shell, cross-shell excitations may occur both out of the lower $p$ shell and into the upper $pf$ shell. Figure 13 indicates that lower-spin negative-parity states are primarily the former case (well-reproduced by YSOX and FSU calculations incorporating the lower $p$ shell), while higher-spin states are primarily the latter case. To provide further detail, occupancy factors were calculated using the FSU interaction for selected 1-particle 1-hole states, and are shown in Figure 14. At low spin the predominant cross-shell excitation mode is the promotion of a proton out of the lower $p$ shell, usually to the $0d_{5/2}$ orbital. Here proton excitation is favoured due to the lower occupation of the $0d_{5/2}$ orbital for protons compared to neutrons near the ground state. With $I \geq 7/2$ the most common excitation mechanism becomes promotion of a neutron out of the

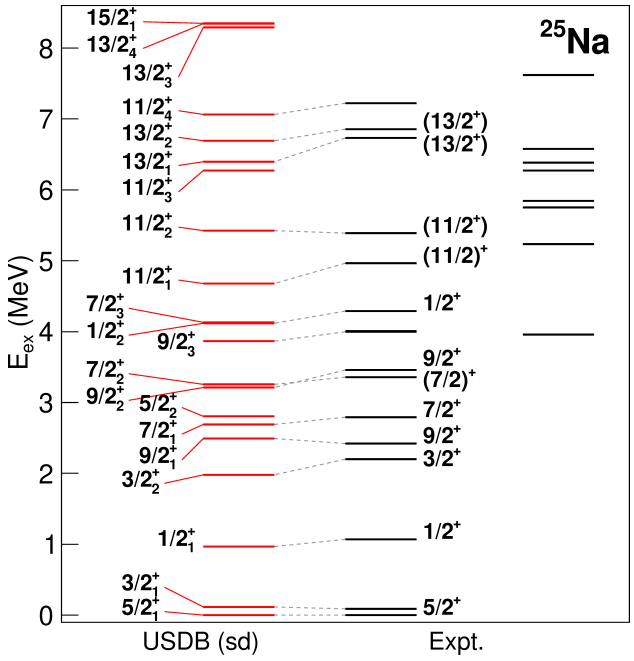


FIG. 12. Comparison of experimentally observed levels in $^{25}$Na to calculations using the USDB interaction, with dashed lines connecting analogous levels. The remaining experimental data is compared to negative-parity levels predicted using the YSOX, SDPF-MU, and FSU interactions in Figure 13.

TABLE IV. Comparison of experimentally obtained $B(E1)$ values for select transitions in $^{25}$Na to predictions using the SDPF-MU interaction. Experimental $B(E1)$ values are limits assuming no $M2$ mixing and with the $11/2^-_1$ level at 6581(2) keV.

| Transition | $B(E1)$ $(e^2fm^2)$ | |
|---|---|---|
| | This work | SDPF MU |
| $\frac{11}{2}^-_1 \rightarrow \frac{9}{2}^+_1$ | $> 2.17 \times 10^{-4}$ | $3.604 \times 10^{-6}$ |
| $\frac{11}{2}^-_1 \rightarrow \frac{9}{2}^+_2$ | $> 5.15 \times 10^{-4}$ | $4.521 \times 10^{-6}$ |
| $\frac{13}{2}^-_1 \rightarrow \frac{11}{2}^+_1$ | $> 4.44 \times 10^{-4}$ [a] | $1.429 \times 10^{-6}$ |
| $\frac{11}{2}^-_2 \rightarrow \frac{11}{2}^+_1$ | $> 4.44 \times 10^{-4}$ [b] | $2.976 \times 10^{-9}$ |

[a] Assuming the level at 7626(4) keV is $I^\pi = 13/2^-_1$.
[b] Assuming the level at 7626(4) keV is $I^\pi = 11/2^-_2$.

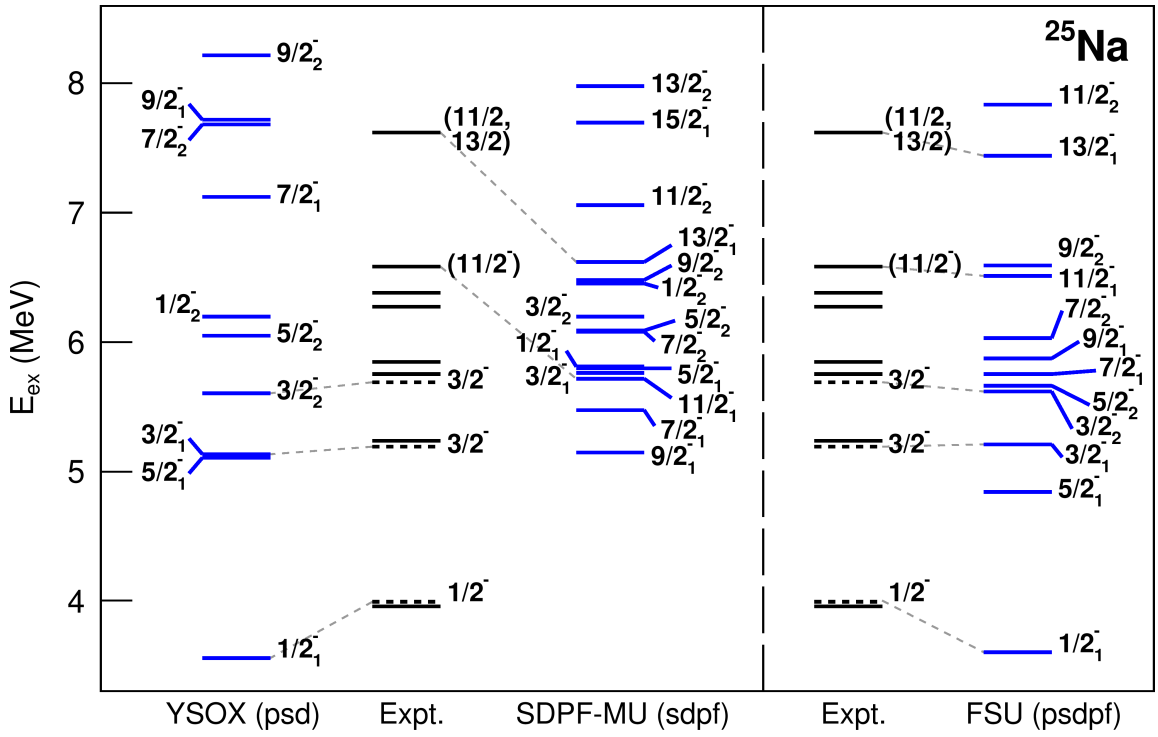


FIG. 13. Comparison of select experimentally observed levels in $^{25}$Na to negative-parity levels calculated using the YSOX, SDPF-MU, and FSU (truncated to *psdpf*) interactions. Additional negative-parity levels from Ref. [28] are shown alongside the experimental data using dashed lines.

*sd* shell, mostly to the $0f_{7/2}$ orbital.

For the positive-parity states, transition strengths calculated using the USDB, YSOX, and SDPF-MU interactions generally agree well with the experimental data, as shown in Table V.

### B. $^{22}$Ne

The known positive-parity levels of $^{22}$Ne are very well reproduced by the USDB calculations, as shown in Figure 15. At high excitation energy, the observed levels with $I^\pi = (7_1^+)$, $(8_1^+)$ also agree well with the USDB predictions. Negative-parity states were calculated using the YSOX and FSU interactions, shown in Figure 16.

There are some candidates for higher-spin negative-parity states in $^{22}$Ne. As Figure 16 shows, the observed levels at 6841(7), 8460(3), and 9161(5) keV approximately correspond in excitation energy to predicted $2_2^-$, $5_1^-$, and $4_2^-$ levels using the YSOX interaction, taking into account an energy offset seen between predicted and observed energies for the lower-lying negative-parity levels. The ordering of levels predicted by the FSU interaction differs somewhat, where the same observed levels instead agree closest with predicted $2_2^-$ or $3_2^-$, $5_1^-$, and $4_4^-$ levels. Alternatively, the 8460(3) keV level may correspond to the $4_5^+$ (8381 keV) level predicted in the USDB calculations (the $4_4^+$ level is likely the level observed at 7337(2) keV, with a predicted energy of 7082 keV in the USDB calculations). Another disagreement between the models is seen for the known $3^-$ level at 7723(2) keV: in the YSOX calculations the observed level most closely

TABLE V. Comparison of experimentally obtained $B(E2)$ and $B(M1)$ values for select transitions in $^{25}$Na to predictions using the USDB, YSOX, and SDPF-MU interactions (with $g_s^{eff} = g_s^{free}$ for calculated $B(M1)$ values). Experimental $B(M1)$ values are limits assuming no $E2$ mixing, with $11/2_1^+$ and $13/2_1^+$ levels at 5388.4(18) and 6736.6(19) keV respectively.

| Transition | $B(E2)$ $(e^2fm^4)$ | | | | |
|---|---|---|---|---|---|
| | This work | VonMoss *et al.* [8] | USDB | YSOX | SDPF MU |
| $\frac{9}{2}^+_1 \rightarrow \frac{5}{2}^+_1$ | 43(9) | 41(7) | 54 | 42 | 41 |
| $\frac{9}{2}^+_2 \rightarrow \frac{9}{2}^+_1$ | $< 4.17 \times 10^3$ | $< 6.99 \times 10^3$ | 28.2 | 25.2 | 11.5 |

| Transition | $B(M1)$ $(\mu_N^2)$ | | | | |
|---|---|---|---|---|---|
| | This work | VonMoss *et al.* [8] | USDB | YSOX | SDPF MU |
| $\frac{7}{2}^+_1 \rightarrow \frac{5}{2}^+_1$ | $< 2.0 \times 10^{-2}$ | $< 1.6 \times 10^{-2}$ | 0.005 | 0.021 | 0.03 |
| $\frac{9}{2}^+_2 \rightarrow \frac{9}{2}^+_1$ | $< 0.32$ | $< 0.53$ | 0.22 | 0.24 | 0.15 |
| $\frac{11}{2}^+_1 \rightarrow \frac{9}{2}^+_2$ | $< 0.25$ | $< 0.19$ | 0.09 | 0.082 | 0.06 |

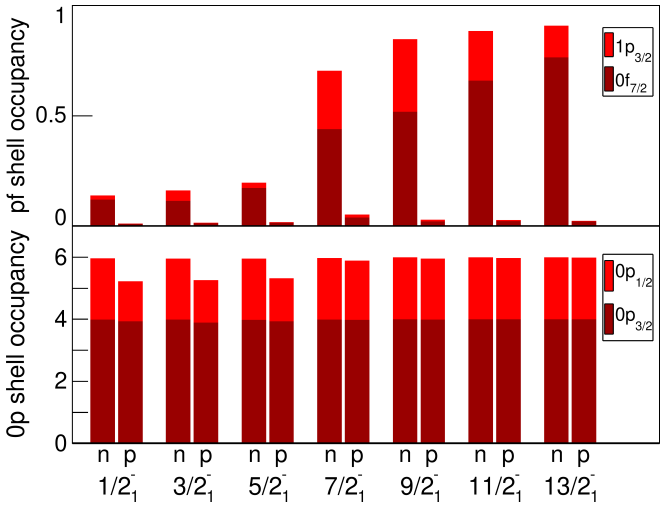


FIG. 14. (Color online) Proton and neutron occupancies calculated for selected 1-particle 1-hole states in $^{25}$Na, using the FSU interaction truncated to the *psdpf* space. Orbitals with proton and neutron occupancies in the lower $p$ and the upper $fp$ shells, which play the dominant role in the $1p1h$ excitations, are shown.

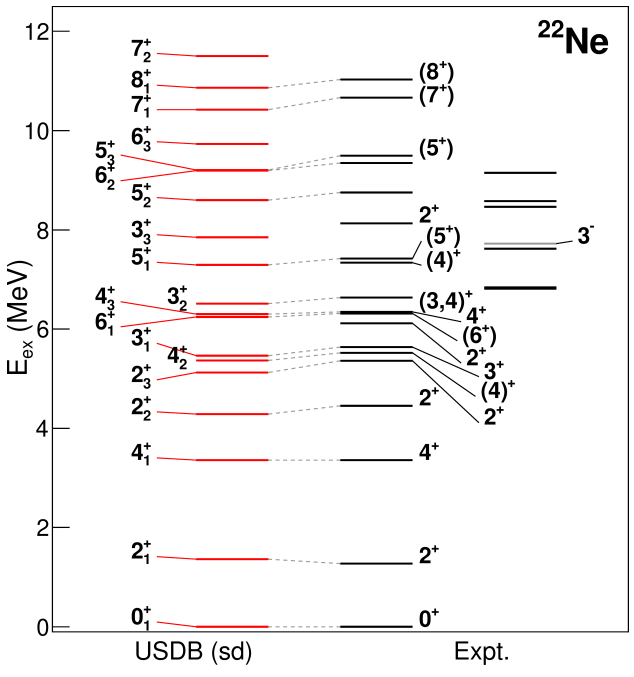


FIG. 15. Comparison of experimentally observed levels in $^{22}$Ne to calculations using the USDB interaction, with dashed lines connecting analogous levels. The remaining experimental data is compared to negative-parity levels predicted using the YSOX and FSU interactions in Figure 16.

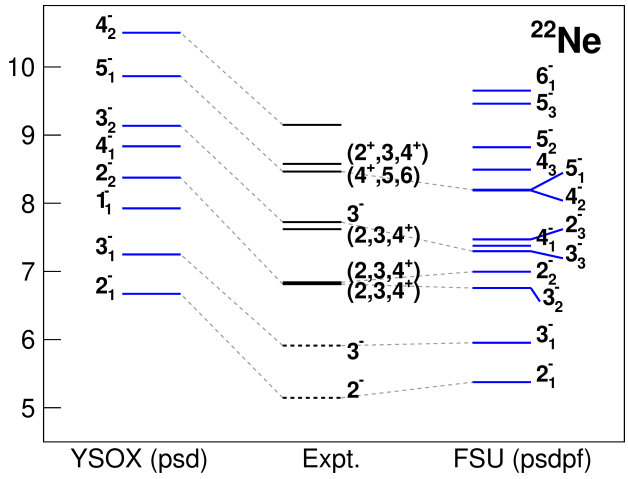


FIG. 16. Comparison of select experimentally observed levels in $^{22}$Ne to negative-parity levels calculated using the YSOX and FSU (truncated to *psdpf*) interactions. Additional negative-parity levels from Ref. [29] are shown alongside the experimental data using dashed lines.

matches the predicted $3^-_2$ level, whereas in the FSU calculations the closest match is the predicted $3^-_3$ level, with the predicted $3^-_2$ level more closely matching either of the levels observed at 6812.8(17) or 6841(7) keV.

For the positive-parity states along the yrast band, $B(E2)$ values determined in this study are in good agreement with the USDB predictions as shown in Figure 17. The YSOX predictions are in better agreement with the evaluated data of Ref. [29], with slightly lower transition strengths compared to the USDB model but a similar overall trend with increasing spin.

## V. SUMMARY

The level schemes of $^{25}$Na and $^{22}$Ne have been extended in the high energy/high-spin regime. The results obtained in this study show very good agreement with USDB predictions for positive-parity states, with mixed results for negative-parity states when comparing to predictions using the YSOX interaction in the *psd* space and the SDPF-MU interaction in the *sdpf* space. Calculations using the FSU interaction in the *psdpf* space provide additional evidence for cross-shell excitations in $^{25}$Na either out of the lower $p$ shell or into the upper $pf$ shell, when compared to the current and previous data.

The results obtained in this study demonstrate the utility of high-spin reactions for challenging existing shell models. Even in the case of nuclides at or near stability, which are easily populated through other means and have been well-studied in the low-spin regime, higher-spin states serve as a useful benchmark for models which handle cross-shell excitations. For $^{25}$Na, nominally a mid-*sd* shell nucleus, there is significant evidence of neu-

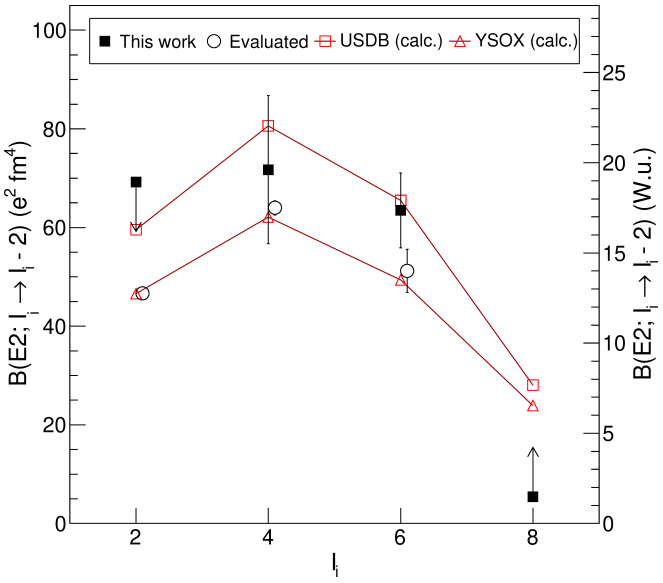


FIG. 17. Comparison of experimentally obtained $B(E2)$ values for the main band of $^{22}$Ne to predictions using the USDB and YSOX interactions. Evaluated data is taken from Ref. [29].

tron excitation into the $pf$ shell at high excitation energy. The methods used in this study could be extended to further investigate the evolution of shell closures, particularly in cases where direct access to closed-shell nuclides is prohibitively difficult due to low reaction cross-sections and/or the need for intense rare isotope beams.

## ACKNOWLEDGMENTS

The authors acknowledge the support of the ISAC Operations Group at TRIUMF, and the Simon Fraser University Electronics and Machine Shops. This work was supported by the Natural Sciences and Engineering Research Council of Canada, the Canadian Foundation for Innovation and the British Columbia Knowledge Development Fund. TRIUMF receives federal funding through a contribution agreement with the National Research Council of Canada. This work was supported in part by a research grant from the Science and Engineering Research Board (SERB) of India (CRG/2019/000556). All FSU shell model calculations were performed using the computational facility of the nuclear physics theory group, Florida State University, supported by a grant from the U.S. Department of Energy, Office of Science (DE-SC-0009883 (FSU)).

[1] T. Otsuka, T. Suzuki, R. Fujimoto, H. Grawe, and Y. Akaishi, Physical Review Letters **95**, 232502 (2005).
[2] E. K. Warburton, J. A. Becker, and B. A. Brown, Physical Review C **41**, 1147 (1990).
[3] Y. Utsuno, T. Otsuka, T. Mizusaki, and M. Honma, Physical Review C **60**, 054315 (1999).
[4] A. N. Deacon, J. F. Smith, S. J. Freeman, R. V. F. Janssens, M. P. Carpenter, B. Hadinia, *et al.*, Physical Review C **82**, 034305 (2010).
[5] S. S. Bhattacharjee *et al.*, Physical Review C **89**, 024324 (2014).
[6] R. Dungan, S. L. Tabor, R. S. Lubna, A. Volya, V. Tripathi, B. Abromeit, D. D. Caussyn, K. Kravvaris, and P.-L. Tai, Physical Review C **94**, 064305 (2016).
[7] J. Williams, G. C. Ball, A. Chester, T. Domingo, A. B. Garnsworthy, G. Hackman, *et al.*, Physical Review C **100**, 014322 (2019).
[8] J. M. VonMoss *et al.*, Physical Review C **92**, 034301 (2015).
[9] H. P. Trautvetter, M. Wiescher, K. U. Kettner, C. Rolfs, and J. W. Hammer, Nuclear Physics A **297**, 489 (1978).
[10] A. Best, S. Falahat, J. Görres, M. Couder, R. deBoer, R. T. Güray, *et al.*, Physical Review C **87**, 045806 (2013).
[11] U. Giesen *et al.*, Nuclear Physics A **567**, 146 (1994).
[12] C. Broude, W. G. Davies, J. S. Forster, and G. C. Ball, Physical Review C **13**, 953 (1976).
[13] K. L. Keyes *et al.*, Journal of Physics G: Nuclear and Particle Physics **31**, S1903 (2005).
[14] G. Hackman and C. E. Svensson, Hyperfine Interactions **225**, 241 (2014).
[15] J. Williams *et al.*, Nuclear Instruments and Methods in Physics Research Section A **939**, 1 (2019).
[16] P. Voss *et al.*, Nuclear Instruments and Methods in Physics Research Section A **746**, 87 (2014).
[17] W. D. Hamilton, *The Electromagnetic Interaction in Nuclear Spectroscopy* (North-Holland Publishing Company, 1975) pp. 311–339.
[18] S. Agostinelli *et al.*, Nuclear Instruments and Methods in Physics Research Section A **506**, 250 (2003).
[19] A. Chester *et al.*, Nuclear Instruments and Methods in Physics Research Section A **882**, 69 (2018).
[20] J. Williams *et al.*, Nuclear Instruments and Methods in Physics Research Section A **859**, 8 (2017).
[21] ICRU Report 73, Journal of the ICRU **5**, 1 (2005).
[22] J. F. Ziegler, M. D. Ziegler, and J. P. Biersack, Nuclear Instruments and Methods in Physics Research Section B **268**, 1818 (2010).
[23] J. S. Forster, D. Ward, H. R. Andrews, G. C. Ball, G. J. Costa, W. G. Davies, and I. V. Mitchell, Nuclear Instruments and Methods **136**, 349 (1976).
[24] J. S. Forster, T. K. Alexander, G. C. Ball, W. G. Davies, I. V. Mitchell, and K. B. Winterbon, Nuclear Physics A **313**, 397 (1979).
[25] T. K. Alexander, G. C. Ball, W. G. Davies, and J. S. Forster, Nuclear Physics A **313**, 425 (1979).
[26] R. L. Kozub *et al.*, Nuclear Physics A **403**, 155 (1983).
[27] A. Knapton, *Structure of $^{25}$Na measured using $d(^{24}$Na,$p)^{25}$Na with a radioactive $^{24}$Na beam* (PhD thesis, University of Surrey, 2017).
[28] R. B. Firestone, Nuclear Data Sheets **110**, 1691 (2009).
[29] M. S. Basunia, Nuclear Data Sheets **127**, 69 (2015).
[30] A. B. Garnsworthy *et al.*, Nuclear Instruments and Meth-

ods in Physics Research Section A **918**, 9 (2019).
[31] E. Krämer, G. Mairle, and G. Kaschl, Nuclear Physics A **165**, 353 (1971).
[32] J. Jänecke, Nuclear Physics A **204**, 497 (1973).
[33] L. D. Olivier, W. A. Richter, J. A. Stander, and J. W. Koen, Zeitschrift für Physik A **347**, 99 (1993).
[34] L. K. Fifield, R. W. Zurmühle, D. P. Balamuth, and S. L. Tabor, Physical Review C **13**, 1515 (1976).
[35] C. N. Davids, D. R. Goosman, D. E. Alburger, A. Gallmann, G. Guillaume, D. H. Wilkinson, and W. A. Lanford, Physical Review C **9**, 216 (1974).
[36] S. Hinds, H. Marchant, and R. Middleton, Proceedings of the Physical Society **78**, 473 (1961).
[37] B. A. Brown and W. A. Richter, Physical Review C **74**, 034315 (2006).
[38] C. Yuan, T. Suzuki, T. Otsuka, F. Xu, and N. Tsunoda, Physical Review C **85**, 064324 (2012).
[39] Y. Utsuno, T. Otsuka, B. A. Brown, M. Honma, T. Mizusaki, and N. Shimizu, Physical Review C **86**, 051301(R) (2012).
[40] R. S. Lubna *et al.*, Physical Review C **100**, 034308 (2019).
[41] R. S. Lubna, K. Kravvaris, S. L. T. V. Tripathi, E. Rubino, and A. Volya, arXiv:2002.01991 [nucl-ex].